POLARIMETRY AND THE HIGH-ENERGY EMISSION MECHANISMS IN QUASAR JETS: THE CASE OF PKS 1136−135.

Mihai Cara[1,2], Eric S. Perlman[1], Yasunobu Uchiyama[3], Chi C. Cheung[4], Paolo S. Coppi[5], Markos Georganopoulos[6], Diana M. Worrall[7], Mark Birkinshaw[7], William B. Sparks[8], Herman L. Marshall[9], Lukasz Stawarz[10,11], Mitchell C. Begelman[12], Christopher P. O'Dea[13], Stefi A. Baum[14]

ABSTRACT

Since the discovery of kiloparsec-scale X-ray emission from quasar jets, the physical processes responsible for their high-energy emission have been poorly defined. A number of mechanisms are under active debate, including synchrotron radiation, inverse-Comptonized CMB (IC/CMB) emission, and other Comptonization processes. In a number of cases, the optical and X-ray emission of jet regions are inked by a single spectral component, and in those, high- resolution multi-band imaging and polarimetry can be combined to yield a powerful diagnostic of jet emission processes. Here we report on deep imaging photometry of the jet of PKS 1136−135 obtained with the *Hubble Space Telescope.* We find that several knots are highly polarized in the optical, with fractional polarization $\Pi > 30\%$. When combined with the broadband spectral shape observed in these regions, this is very difficult to explain via IC/CMB models, unless the scattering particles are at the lowest-energy tip of the electron energy distribution, with Lorentz factor $\gamma \sim 1$, and the jet is also very highly beamed ($\delta \geq 20$) and viewed within a few degrees of the line of sight. We discuss both the IC/CMB and synchrotron interpretation of the X-ray emission in the light of this new evidence, presenting new models of the spectral energy distribution and also the matter content of this jet. The high polarizations do not completely rule out the possibility of IC/CMB optical-to-X-ray emission in this jet, but they do strongly disfavor the model. We discuss the implications of this finding, and also the prospects for future work.

Keywords: galaxies: jets — quasars : individual (PKS 1136−135) — quasars : general — polarization — magnetic fields

1. INTRODUCTION

The jets of radio-loud Active Galactic Nuclei (AGN) carry energy and matter out from the nucleus to cluster-sized lobes, over distances of hundreds of kpc. While found in only $\sim 10\%$ of AGN, jets can have a power

[1] Department of Physics and Space Sciences, Florida Institute of Technology, 150 W. University Blvd., Melbourne, FL 32901, USA
[2] Current Address: Physics Department, Case Western Reserve University, 2076 Adelbert Rd., Cleveland, OH, 44106-7079
[3] SLAC/KIPAC, Stanford University, 2575 Sand Hill Road, M/S 209, Menlo Park, CA 94025, USA
[4] Space Science Division, Naval Research Laboratory, Washington, DC 20375, USA
[5] Yale University, Department of Astronomy, PO Box 208101, New Haven, CT 06520-8101
[6] Department of Physics, University of Maryland – Baltimore County, 1000 Hilltop Circle, Baltimore, MD 21250, USA
[7] Department of Physics, University of Bristol, Bristol, BS8 1TL, UK
[8] Space Telescope Science Institute, 3700 San Martin Drive, Blatimore, MD 21218, USA
[9] Kavli Institute for Astrophysics and Space Research, Massachusetts Institute of Technology, Cambridge, MA 02139, USA
[10] Institute of Space Astronautical Science, JAXA, 3-1-1 Yoshinodai, Chuo-Ku, Sagamihara, Kanagawa 252-5210, Japan
[11] Astronomical Observatory, Jagiellonian University, 30-244 Krakow, Poland
[12] Department of Astrophysical and Planetary Sciences, UCB 391, University of Colorado, Boulder, CO 80309-0391
[13] Laboratory for Multiwavelength Astrophysics, School of Physics and Astronomy, Rochester Institute of Technology, 84 Lomb Memorial Dr., Rochester, NY 14623-5603
[14] Chester F. Carlson Center for Imaging Science, Rochester Institute of Technology, 54 Lomb Memorial Dr., Rochester, NY 14623-5604

output (including both luminosity and kinetic energy flux) comparable to that of their host galaxies and AGN (Rawlings 1991), and can profoundly influence the evolution of the hosts and neighbors (McNamara & Nulsen 2007). AGN jets are completely ionized flows, and the radiation we see from them is non-thermal in nature. The highest-power radio jets typically terminate in bright "hot-spots" and are classified as Fanaroff-Riley type II (FR II) while the lower-power radio-jets are brightest at the core and are classified as Fanaroff-Riley type I (FR I) (Fanaroff & Riley 1974). That the radio emission arises from synchrotron radiation is supported by strong linear polarization and power-law spectra seen in both lower- and higher-power jets. However, in the optical and X-ray bands, the nature of the emission from higher-power large-scale jets is less clear.

In low-power FR I radio galaxies, the optical and X-ray fluxes fit on extrapolations of the radio spectra (see e.g., Perlman et al. 2001; Hardcastle et al. 2001; Perlman & Wilson 2005), and high polarizations are seen in the optical (typically $\sim 20 - 30\%$, Perlman et al. 1999, 2006) suggesting synchrotron emission. These jets exhibit a wide variety of polarization properties (Perlman et al. 2006; Dulwich et al. 2007; Perlman et al. 2010), often correlated with X-ray emission. For example, in the jet of M87 (Perlman & Wilson 2005), a strong anti-correlation between the intensity of X-ray emission and optical polarization fraction was found in the knots, accompanied by changes in the magnetic field direction, suggesting a strong link between the jet's dynamical structure and high-energy processes in the jet interior, where shocks compress the magnetic field and

accelerate particles.

For the more powerful FR II and quasar jets, the nature of both the optical and X-ray emission is under active debate. The first issue to resolve is whether the mechanism and electron population that produces optical emission is linked with the radio or X-ray emission. For some knots in FR II jets, the radio-to-X-ray SED is consistent with the optical and X-ray arising as synchrotron from the same electron population as that producing the radio emission (see e.g., Worrall & Birkinshaw 2005; Kraft et al. 2005; Kataoka et al. 2008). In others, however, the optical emission can lie well below an interpolation between the radio and X-rays (e.g., Sambruna et al. 2004), sometimes by decades (e.g., PKS 0637−752, Schwartz et al. 2000; Mehta et al. 2009), resulting in a characteristic double-humped shape of spectral energy distribution. In some jets the optical emission appears linked to the X-ray emission by a common component, as seen in both 3C 273 and PKS 1136−135, where deep Hubble Space Telescope (HST), Chandra X-ray Observatory and infrared Spitzer Space Telescope imaging (Jester et al. 2001, 2006, 2007; Uchiyama et al. 2006, 2007) has shown that a second component, distinct from the lower-energy synchrotron emission, arises in the near-IR/optical and dominates the jet emission at optical and higher energies, at least up to $10 \, \mathrm{keV}$. Competing mechanisms have been proposed: either synchrotron radiation from very high-energy particles or inverse-Comptonization of low energy photons off relativistic electrons of the jet (see Kataoka & Stawarz 2005; Harris & Krawczynski 2006; Worrall 2009), however, the nature of this component cannot be constrained by multi-waveband spectra alone (Georganopoulos et al. 2006).

Polarimetry is a powerful diagnostic for jets because synchrotron emission is naturally polarized, with the inferred direction of the magnetic field vector indicating the weighted direction of the magnetic field in the radiating volume and the fractional polarization indicating relative ordering of the magnetic field. In FR IIs, where the radio-optical spectrum often cannot be extrapolated to the X-rays, high-energy synchrotron emission is a possibility, but often requires a second electron population. For FR IIs to accelerate particles to $\gamma > 10^7$, as required for X-ray synchrotron emission, requires highly efficient particle acceleration mechanisms that can operate well outside the host galaxy (e.g., in PKS 1136−135 the X-ray emitting knots are at projected distances of $30 - 60 \, \mathrm{kpc}$ from the AGN). If the optical and X-ray emission is synchrotron radiation, the optical polarization will be high, comparable to that seen in the radio, but with characteristics that may be linked to acceleration processes.

The second possibility is inverse-Comptonization of Cosmic Microwave Background photons (IC/CMB, Celotti et al. 2001). This requires a jet that remains highly relativistic out to distances of hundreds of kpc (Schwartz et al. 2000; Tavecchio et al. 2000; Georganopoulos & Kazanas 2003), viewed at a small angle to the line of sight. Any optical IC-CMB would be linked to nearly cold electrons, with $\gamma < 10$, a population of particles that has never before been tracked. If the emitter is moving at relativistic bulk speeds, $\Gamma \gg 1$, then the forward-bunching effect will make the CMB photons essentially unidirectional in the jet frame.

The IC scattering on the unidirectional and unpolarized photon beam by high-energy electrons having large Lorentz factors ($\gamma \gg 1$) should be unpolarized. On the other hand, the scattered radiation from cold electrons ($\gamma \sim 1$; so-called vulk Comptonization) in the jet is expected to be highly polarized (Begelman & Sikora 1987). Uchiyama & Coppi (2013) have carried out calculations covering the intermediate regime with $\gamma \sim$ few, making use of the general expression for the intensity and polarization of singly-scattered Comptonized radiation presented by Poutanen (1993). They found that, for a power-law energy distribution of electrons with a cutoff at $\gamma_{\min} = 2$, the polarization degree can be as large as 8% with the direction of the electric field vector perpendicular to the jet axis (see also McNamara et al. 2009).

It is also possible to Comptonize other photon fields. The most commonly cited process is synchrotron self-Compton (SSC) radiation, in which the seed photons come from the jet's low-frequency radio emission. While SSC is unavoidable, it is unlikely to dominate the X-ray emission of the jet knots because in order to fit the observed X-ray emission, one requires a jet that is massively out of equipartition (by factors of $20 - 100$), has large viewing angle and/or is unbeamed. However, SSC is the leading scenario for X-ray emission from the terminal hotspots of the most powerful jets (Harris et al. 1994; Wilson et al. 2001). SSC predicts optical polarization properties similar to that of the lowest-frequency radio emission.

All of these issues have important implications on the overall mass-energy budget and energetics of powerful jets. For example, a large population of nearly cold electrons could carry the vast majority of the matter content and energy budget of the jet, making them vital in constraining the overall energetics of the jet. A second factor, which is even more difficult to constrain, would be whether the jet flow is composed purely of leptons, or includes hadrons (e.g., Georganopoulos et al. 2005). If either of these components is found, the jet flow could become more powerful by orders of magnitude, resulting in a much greater impact on the surrounding ICM and more extreme demands on the overall physics (e.g., Ghisellini & Celotti 2001).

Up until now the only existing optical polarimetric observations of quasar jets were those of the quasar 3C 273, where ground based polarimetry (Röser & Meisenheimer 1991) yielded significantly different results from (pre-COSTAR FOC) space-based observations with HST (Thomson et al. 1993). The discrepancy could not be reconciled by simply accounting for differences in resolution. In this paper we present, for the first time, high-resolution space-based optical polarimetric observations of the quasar jet PKS 1136−135.

PKS 1136−135 is a steep-spectrum quasar at $z = 0.556$. It has a low integrated optical polarization $< 1\%$ (Sluse et al. 2005). It is part of the 2 Jy sample (Wall & Peacock 1985), and spectroscopy and images of its host galaxy were presented by Tadhunter et al. (1993) and Ramos Almeida et al. (2011) respectively. It was selected for inclusion in a search for X-ray jet sources based on the brightness of its radio jet by Sambruna et al. (2002), whose short X-ray observation with *Chandra* was supplemented with a wide-band *HST* image. Later, deeper *Chandra* and *HST* observations

were analyzed by Sambruna et al. (2006). Its X-ray jet features emission from five regions of the jet, plus the terminal hotspot. Modeling of the jet SED by Sambruna et al. (2006), which assumed IC/CMB for the jet X-ray emission mechanism, found a Doppler factor $\delta \sim 7$. Thanks to data from the *VLA, HST* and *Chandra*, as well as *Spitzer*, the spectral energy distribution (SED) of its jet is the best sampled among the lobe-dominated quasars. The jet has a morphology similar to that seen in 3C 273, displaying an anti correlation between radio and X-ray flux. This has been interpreted as being indicative of deceleration (Sambruna et al. 2006; Tavecchio et al. 2006).

The paper is laid out as follows. In Section 2, we describe the observations and data reduction methods. Section 3 describes the morphology, polarimetry and spectral imaging results we obtain for PKS 1136−135. Section 4 describes model fitting and a discussion of the implications of these results. Finally we close in Section 5 by stating our conclusions. Throughout this paper we assume a cosmology with $\Omega_m = 0.27$, $\Omega_\Lambda = 0.73$, $\Omega_r = 0$ and $H_0 = 71$ km s^{-1} Mpc^{-1}. For PKS 1136−135 this leads to a luminosity distance of 3.20 Gpc, and an angular scale of $1'' = 6.4$ kpc. We also adopt the following convention for the spectral index, α: $F_\nu \propto \nu^{-\alpha}$, where ν is the frequency.

2. OBSERVATIONS AND DATA REDUCTION

2.1. *Polarimetric Observations*

Optical polarimetry of the jet of the quasar PKS 1136−135 was performed (proposal #11138, Cycle 16) with HST's Wide Field and Planetary Camera 2 (WFPC2) between March 2 and March 16, 2008 using the Wide Field (WF) chips of the WFPC2 camera with the F555W (broadband V) and POLQ filters. To reconstruct the Stokes parameters, it is necessary to observe a source using different polarizer orientations. However, as the polarizer can rotate through only 51°, rotating the polarizer results in a very small field of view. We therefore followed the practice of Perlman et al. (1999, 2006) and obtained images in all three WF chips (WF2, WF3, and WF4) for which the polarizer has a nominal orientation of 0°, 45°, 90° respectively, where an orientation of 0° lies roughly along the $+X$ direction of the PC1 chip (This corresponds to values of 45°, 90°, and $135° - PA\_V3$ with respect to North, where PA_V3 is the angle between North and the $V3$ axis of the telescope; see Biretta & McMaster 1997 for more details). The observations were performed in 21 orbits (exposure time of 2500 seconds per orbit) evenly split between WF chips for a total of 17500 seconds of exposure time per polarizer orientation giving us the deepest optical image of the PKS 1136−135 jet to date. We used a simple line-dither pattern for our observations which allowed for a better recovery of information in the defective/hot pixels and pixels affected by cosmic rays (CR). The F555W filter was chosen for the following reasons: i) based on pre-existing photometry, its pivot wavelength falls inside the "dip" between the low-energy (radio to infrared) and the high-energy (optical to X-ray) bumps of the broadband spectrum thus minimizing the contribution from the low-energy (synchrotron) component to the total flux and polarization; ii) it complements existing non-polarimetric

observations at other optical wavelengths (*HST* F475W, F625W, F814W; see Sambruna et al. 2006); iii) it provides optimal performance of the POLQ filters (i.e., maximized parallel and minimized perpendicular transmissions).

2.2. *Image Processing*

As the first step, we re-calibrated the images using the most up-to-date reference files (i.e., flat field files, distortion correction table, etc.) obtained from the STScI Calibration Database System. In addition to this standard calibration procedure, we have re-computed the PHOTFLAM and PHOTPLAM keyword values using the `calcphot` routine from the `SYNPHOT` package assuming a power-law spectral distribution with a spectral index $\alpha_{\rm rad} = 1$. We used the `Multidrizzle` task (Fruchter et al. 2009) from the `STSCI_PYTHON` package to drizzle-combine the images for each polarizer orientation (WF chip). Besides combining the images, `Multidrizzle` distortion-corrects the images, performs image flat-fielding, cosmic-ray rejection, image alignment, and other tasks.

However, in order to obtain good final drizzle-combined images, it is necessary to supply good image alignment information to the `Multidrizzle` task. To find the necessary geometric transformations we used an iterative process so that after each iteration we have obtained an improved estimate for image shifts and rotations. This process was done as follows. At first, we individually drizzled all images onto a common frame and, using the positions of the same star-like object in each drizzled image, we found an *initial* estimate of the shifts necessary to align the images (no rotations or distortions were considered at the initial stage). We then set up the following iterative process:

i) we use `Multidrizzle` with the available geometric transformations (in the form of a "shifts file") to perform distortion correction and clean cosmic rays from the images;

ii) on these images we run the `Tweakshifts` task (a part of the `STSCI_PYTHON` package) to find the *delta*-shifts and rotations between images using 13 reference objects (stars and unresolved clusters). `Tweakshifts` automatically excludes the objects that cannot be fit well with a best fit model for geometric transformations;

iii) we update the old shifts file with delta-shifts found in the previous step and repeat this process starting with step i) until we obtain corrections to shifts and rotations smaller than 10^{-3} pixels and 10^{-4} degrees accordingly.

Decreasing values of the corrections are an indication of convergence of the iterative process. However, these corrections are not an indication of goodness of alignment. For this, we use the root mean square of the residuals of the fit as reported in the transformations database created by the `geomap` task which is used internally by the `Tweakshifts` task. More precisely, we define misalignment error as

$$\sigma_{\rm fit} = \sqrt{\frac{1}{N-1} \sum_{i=2}^{N} ((\sigma^i_{x,{\rm fit}})^2 + (\sigma^i_{y,{\rm fit}})^2)}, \qquad (1)$$

where $\sigma_{x,\mathrm{fit}}^{i}$ and $\sigma_{y,\mathrm{fit}}^{i}$ are coordinate residuals of the fit as reported in the `geomap`'s database file. Index i numbers input images to the `Tweakshifts` task. Since the alignment is performed relative to the first input image, the summation in the above equation is performed over index i that runs from 2 to N. For WFPC2 F555W+POLQ data the estimated misalignment error was 0.16 pixels and at this level it was shown (Perlman et al. 2006) to have a minor effect on polarimetry (this effect is further minimized in the case of *aperture* polarimetry). By performing the image alignment procedure *simultaneously* on all input images regardless of their epoch or polarization filter, we avoid an extra step of aligning drizzled images from the three polarizers (images with different polarizer filters must be aligned to obtain Stokes images later) – a step that would have led to degradation of the image quality.

With the shift information from the image alignment step, we then combined images with the same POLQ filter using the `Multidrizzle` task. At first, we performed sky background subtraction on the input images using our own routine that can use selected regions of the sky and cosmic ray masks for background evaluation. We then used the `Multidrizzle` task to perform distortion correction of the images, cosmic ray cleaning, rotate images North-up, and drizzle-combine images into a single final image.

2.3. *Polarization Images*

Observations with different polarizer orientations (i.e., different apertures with the POLQ filter) can be linearly combined (see Biretta & McMaster 1997) to produce Stokes I, Q, and U images:

$$\mathbf{S} = M\mathbf{W}, \qquad (2)$$

where $\mathbf{S} = (I, Q, U)$ is a vector of Stokes images and $\mathbf{W} = (W_2, W_3, W_4)$ is a vector of WFPC2 images corresponding to different polarizer orientations (in our case WF2, WF3, and WF4 CCD chips with POLQ filter). Coefficients of the Mueller matrix M were computed using the WFPC2 Polarization Calibration Tool[15]. Prior to combining the images using matrix M, it is necessary to check that all images have similar resolution (differences in resolution could be due to telescope optics, quality of shifts used by `Multidrizzle`, jitter, and other factors). This was done by measuring the Gaussian FWHM of 3–4 sharpest globular clusters in the drizzle-combined images using the `imexamine` task and taking their average value. The WF4 image had the largest averaged FWHM equal to $0''.1889$. Therefore, we applied a Gaussian blur filter of appropriate standard deviation to the WF2 and WF3 images so as to make their average FWHM match that of the WF4 image. Finally, we combine the $\mathbf{W}$ images to obtain Stokes images. The resulting image is shown in Figure 1.

As the quasar and host galaxy in PKS 1136−135 are quite bright, their emission almost completely hides the innermost jet knot. Therefore, it is important to perform galaxy subtraction prior to any polarimetric measurements, and also mask out the diffraction spikes. Galaxy subtraction was done on the Stokes I image. First,

we masked out the jet, clusters, and other sources of emission except for the host galaxy. We then used the `ellipse` task to fit elliptical isophotes to the host galaxy image and finally, we used the `bmodel` task to create a Stokes I image of the host galaxy from the fitted isophotes. To produce images of the host galaxy that can be subtracted from the drizzle-combined images, we set components Q and U of the vector $\mathbf{S}$ to 0 (host galaxy emission is unpolarized) and invert equation (2) which will produce three images of the host galaxy as if they were observed in CCD chips WF2, WF3, and WF4. We then subtract these images from the corresponding drizzle-combined image using the `imcalc` task. Finally, we repeat polarization combination (eq. 2), this time with the galaxy-subtracted images as inputs. We combine the resulted Stokes I, Q, and U images in a standard way to produce polarization (P) defined as $P = \sqrt{Q^2 + U^2}$, fractional polarization (Π) defined as $\Pi = P/I$ and electric vector position angle (Ξ) defined as $\Xi = \frac{1}{2}\tan^{-1}(U/Q)$ (or, alternatively, magnetic field position angle (MFPA) defined as MFPA $= \Xi + 90°$).

The errors in the polarization images have been computed using standard error propagation with the errors of the input galaxy- and background-subtracted images estimated as the sum, in quadrature, of the Poisson errors in the original (prior to galaxy and background subtraction) images, standard deviation of the background level (post galaxy subtraction), readout noise, and quantization noise. For this analysis we have ignored any errors in the galaxy model. We also added in quadrature 3% absolute error to fractional polarization to account for uncertainties in polarization calibration (Biretta & McMaster 1997). We accounted for the well-known Rician bias in P (Serkowski 1962) using a Python code adapted from the STECF IRAF package (Hook et al. 2000). This code debiases the P image following Wardle & Kronberg (1974), and calculates the error in PA accounting for the non-Gaussian nature of its distribution (see Naghizadeh-Khouei & Clarke 1993). In performing this calculation, pixels with signal to noise (S/N) < 0.1 were excluded outright, and since the debiasing is done with a most-probable value estimator, pixels where the most probable value of P was negative, or above the Stokes I value (i.e., $\Pi > 100\%$) were blanked. This code was first used in Perlman et al. (2006).

2.4. *Aperture Polarimetry and Photometry*

Aperture polarimetry was performed using rectangular and elliptical regions large enough to include most of the emission from the optical knots. In Figure 1 we show galaxy-subtracted Stokes I image of the quasar jet PKS 1136−135 with green rectangles and a ellipse showing the apertures used in this analysis together with knot nomenclature. Positions and sizes of the apertures have been chosen so that they include the knots but avoid the nearby saturated column, diffraction spikes, and other sources of signal. The larger apertures include most of the flux and thus require minimal aperture correction making the flux values more reliable. However, large apertures tend to produce larger Poisson errors due to inclusion of many low S/N pixels. On the other hand, smaller apertures, while producing higher S/N results, are more susceptible to errors in aperture correction. In

Figure 1 the dashed apertures show the largest apertures used while the continuous line apertures show the location of smaller apertures around the knots. In order to increase the S/N of aperture measurements, we have also used even smaller apertures produced by selecting only 4-point connected pixels with S/N $> 1\sigma$, S/N $> 2\sigma$, and S/N $> 3\sigma$ (we will call these apertures 1σ-cut, 2σ-cut, and 3σ-cut apertures accordingly). Inner holes (if any) are filled-in so that the apertures are simply connected. In Figure 1 we show the 4-point connected apertures with S/N $> 1\sigma$ as red patches. Whenever possible, we have used several apertures of varying size for each knot. For a given knot, the final value for the flux is computed as a weighted mean (Gough 2008):

$$I = \sum_k w_k I_k \qquad (3)$$

and with an error estimate given by:

$$\sigma_I = \sqrt{\frac{1}{1 - \sum_k w_k^2} \sum_k w_k (I - I_k)^2}, \qquad (4)$$

where summation is performed over apertures of different sizes. The weights were chosen as

$$w_k = \frac{1}{(\sigma_k C_k)^2} \left(\sum_k \frac{1}{(\sigma_k C_k)^2} \right)^{-1}, \qquad (5)$$

such that more weight is given to the apertures with smaller measurement (e.g., Poisson errors, read-out noise, etc.) errors (σ_k) and less weight to the apertures with large aperture and CTE correction factors (C_k) described below. The weights in equation (5) have been normalized such that $\sum_k w_k = 1$. Extensive testing showed that the error estimates produced using this method were well justified.

Aperture correction was performed in the following way. We model point-like knots (A, B, and the Hot-Spot) using a PSF generated with the TINYTIM PSF simulation tool[16] (see Krist 1993; Krist & Hook 2004). First, we generated an oversampled ($\times 4$) PSF by providing TINYTIM with knot position, WFPC2 chip, used filter, jitter information extracted from jitter file headers (`jit` files), and set the source spectrum to be a power law with spectral index $\alpha = 1$. Then we rotated and shifted the PSF to the same position and orientation as the knot of interest, re-sampled the PSF to the Stokes I image sampling, and convolved it with a Gaussian kernel with a standard deviation chosen such that the blurred PSF has the same FWHM as the knot (measured with the `imexamine` task). After normalizing the PSF so that total flux is equal to unity, the aperture correction is simply equal to the flux in the PSF that is outside the aperture of interest. With this method we are able to apply aperture corrections to all apertures. For extended knots (α, C, D, and E), which cannot be modeled with the PSF, we use 2σ-cut apertures as model of the knots assuming a constant value for the model flux. We then convolve these models with PSF with a FWHM equal to the FWHM of the unresolved clusters in our image
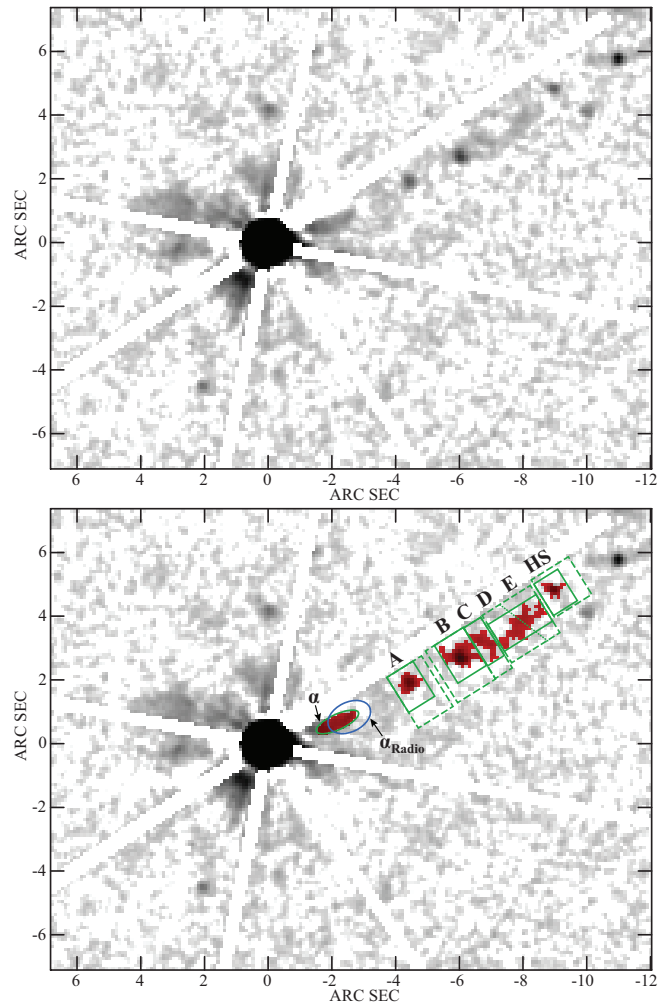

Figure 1. Galaxy subtracted HST F555W Stokes I image of the PKS 1136−135 jet, at top, and at bottom, with knot nomenclature and used apertures superposed. The white regions represent diffraction spike features that have been excluded from our analysis. Dashed green rectangles show the largest apertures. Solid green rectangles and ellipse show smaller apertures. These represent the regions within which pixels were considered for inclusion in various knot regions. The dotted green diagonal line separates knots D and E based on a radio image. The 1σ-cut apertures are shown as red masks overlaid on the jet knots. The blue ellipse shows the location of the knot α in the radio image. See §§ 2.4 and 3.1 for discussion.

($0''.1889$, see § 2.3). For these extended knots, the smallest apertures for which we perform aperture correction are the 1σ-cut apertures. Because of the proximity of the knots α and α_{Radio} to the core and diffraction spikes, we use only the 1σ-cut apertures for flux measurements in these knots.

We correct for charge transfer efficiency (CTE) losses using Dolphin (2009) formulae, which are valid for point sources. We then estimate the CTE correction for extended sources following the recommendations from "WFPC2 Phase II Observation Strategies"[17], more specifically, we divide CTE loss values obtained using Dolphin (2009) formulas by the extent (in native detector pixels) of the knots which we estimate as $\frac{1}{2}\sqrt{N_{\mathrm{pix}}}$, where N_{pix} is the number of pixels in an aperture.

Aperture and CTE corrections are applied to the

---

[16] http://www.stsci.edu/software/tinytim/

[17] http://www.stsci.edu/hst/wfpc2/wfpc2_phase2.html

count-rates in the apertures from each WF CCD image, which are then combined using the same prescription as in § 2.3 to compute Stokes parameters which, in turn, are used to compute P, Π, and EVPA. We correct for the Rician bias and compute errors on polarimetric quantities in a similar fashion to § 2.3. For aperture polarimetry we use the smallest σ-cut apertures for which we could perform aperture correction (3σ-cut apertures for point-like knots A, B, and the Hot Spot, and 1σ-cut apertures for the extended knots). For knots in which the smallest apertures gave zero polarization after debiasing, we used next non-zero aperture for that knot to estimate the upper limit of polarization at the 2σ level.

Normally, to convert a Stokes I count-rate image (or aperture measurements) to flux units we would multiply the count-rate values by the value of the flux unit conversion header keyword PHOTFLAM (U_λ). However, images from different WF CCD chips have different PHOTFLAM and PHOTPLAM (pivot wavelength, λ_P) values, which are also weakly dependent on spectral shape. Since the WFPC2 Polarization Calibration Tool (Biretta & McMaster 1997) assumes count-rates as inputs, we cannot convert input images to flux units and then combine them using equation (2). To deal with this problem we adopt the following strategy of computing "average" PHOTFLAM and PHOTPLAM values. Let $M_{I,k}$ be the coefficients of the matrix M (see eq. 2) used to combine WF2, WF3, and WF4 images (index k runs from 2 to 4) into Stokes I image. Following the expressions for the flux unit conversion factor and pivot wavelength from the "Synphot Users Guide" (see § 7.1 of Laidler 2005), we define "average" PHOTFLAM and PHOTPLAM values as:

$$\langle \lambda_P \rangle = \sqrt{B/A}, \langle U_\lambda \rangle = \frac{1}{B} \sum_{k=2}^{4} M_{I,k}, \qquad (6)$$

where:

$$A = \sum_{k=2}^{4} \frac{M_{I,k}}{\lambda_{P,k}^2 U_\lambda}, B = \sum_{k=2}^{4} \frac{M_{I,k}}{U_\lambda}.$$

We use these averaged PHOTFLAM and PHOTPLAM values to convert Stokes I count-rates to flux units. We also add in quadrature 2% error to the total flux error (see eq. 4) to account for uncertainties in photometric calibration (Baggett et al. 2002).

2.5. HST Photometry With F475W, F625W, and F814W

HST observations and photometry of the PKS 1136−135 jet with F475W, F625W, and F814W filters were performed by Sambruna et al. (2006) (proposal #9682, Cycle 11) using ACS/WFC. We have reprocessed these images and used the data to place better constraints on the optical spectrum and broadband SED of the jet components. However, due to the short exposure time of these observations (676 s for F475W and F625W observations, and 520 s for F814W observations), the S/N in the extended knots is too low to reliably place apertures based on HST images. Because of this, the apertures used for HST photometry in Sambruna et al. (2006) were centered on X-ray/Radio positions. This may be a problem if the location of the

X-ray/Radio knots is different from the location of the optical knots. In Figure 1 the blue ellipse shows the location of the innermost knot α_{Radio} in the radio image (compare with the green ellipse showing the knot α in our deep F555W HST image) and it is clear that optical knot α and radio knot α_{Radio} have different locations. Because of a much higher S/N (exposure time 17500 s per polarizer) of our HST observations, we decided to re-process the earlier F475W, F625W, and F814W observations using the procedure of § 2.4) and apertures as defined in Figure 1.

Since processing of these images followed the same methodology as for our F555W data, we mention here only the differences. First, because F475W, F625W, and F814W observations were CR-SPLIT (and not dithered as were our F555W observations), there was no need to find shifts between input images. Secondly, since the ACS WFC detector's pixel scale is 0.05″ compared to 0.0996″ of the WF detectors, we used the `geomap` and `geotran` tasks to re-scale drizzle-combined images to match the scale of the F555W observations and to align these images to the F555W Stokes I image. Unfortunately, because the F475W, F625W, and F814W observations had only two exposures (input images) per filter, `Multidrizzle` was unable to remove all the cosmic rays from the input images. When these CR where located in some knots, we removed the corresponding pixels from that knot's aperture mask. Also, because of the lack of dithering, the F475W, F625W and F814W data have a significant number of warm/hot pixels and other image defects. Finally, for CTE loss correction we used ACS-specific formulas from the "ACS Data Handbook" (Pavlovsky et al. 2005).

2.6. Chandra X-ray Observations

Observations of the PKS 1136−135 jet were obtained with the Chandra X-ray Observatory on 2003 April 16 (ObsID 3973) by R. Sambruna and collaborators (Sambruna et al. 2006). The total exposure was 77.4 ks. The observations were obtained with ACIS-S, with the sources at the aim point of the S3 chip. The 1/8 subarray mode was used, with a frame time of 0.4s, to minimize the effect of pileup from the quasar itself. The source was also observed at a range of roll angles to place the jet away from the charge transfer tail of the quasar nucleus and avoid flux contamination.

We re-reduced the observations using CIAO version 4.2, with standard screening criteria and calibration files provided by the Chandra X-ray Center. Pixel randomization was removed, and only events in grades 0, $2-4$ and 6 were retained. We also checked for flaring background events. In order to aid comparison to the HST data, we subsampled the native Chandra resolution by 5, leading to a pixel scale of 0.0984″/pixel. In order to maximize the ability to detect low-level extended emission, we smoothed the observations adaptively using csmooth in CIAO, requiring each cell to have a minimum of 10 photons.

Table 1
Flux Densities (F_ν) of Jet Features

Feature	8.5 GHz[a] (mJy)	22 GHz[a] (mJy)	5.8 μm[b] (mJy)	3.6 μm[b] (mJy)	F814W (nJy)	F625W (nJy)	F555W (nJy)	F475W (nJy)	1 keV[a] (nJy)
α	3.0 ± 0.3	1.5 ± 0.6			337 ± 59	330 ± 50	358 ± 16	362 ± 42	1.9 ± 0.2
$\alpha_{\rm Radio}$	3.0 ± 0.3	1.5 ± 0.6			320 ± 60	261 ± 15	249 ± 42		1.9 ± 0.2
A	3.8 ± 0.4	2.0 ± 0.6	< 5	< 4	237 ± 48	208 ± 23	212 ± 14	231 ± 17	1.7 ± 0.2
B	9.3 ± 0.9	3.2 ± 0.6	4.8 ± 2.2	3.8 ± 1.9	535 ± 71	396 ± 35	365 ± 24	320 ± 42	3.5 ± 0.2
C	20.6 ± 2.1	9.2 ± 1.8			342 ± 91	$< 90^a$	148 ± 6	$< 70^a$	1.8 ± 0.2
D	29.5 ± 3.0	11.9 ± 2.4			390 ± 130	191 ± 55	140 ± 17	$< 80^a$	1.0 ± 0.2
E	66.1 ± 6.6	26.4 ± 5.3			161 ± 52	$< 50^a$	130 ± 18	$< 80^a$	0.7 ± 0.2
D+E					500 ± 150		240 ± 30		
C+D+E	$116 \pm 8^{b,c}$	47.5 ± 6.1^b	20 ± 4	9.5 ± 2.0	840 ± 240		383 ± 31		
HS	119 ± 12	43.9 ± 8.8	7.4 ± 2.7	4.6 ± 2.0	287 ± 16	159 ± 33	159 ± 24	115 ± 26	< 0.6

[a] See Sambruna et al. (2006)
[b] From Uchiyama et al. (2007)
[c] Errors recomputed in quadrature

Table 2
Optical and Radio Polarimetry of Jet Features

Feature	R ($''$)	Π_O, %	Ξ_O^a	Π_R, %	Ξ_R^a
α	2.7	$< 15^b$	....	21 ± 2	17 ± 5
$\alpha_{\rm Radio}$		$< 15^b$	....	22 ± 2	19 ± 5
A	4.6	37 ± 6	41 ± 4	11 ± 2	15 ± 5
B	6.5	$< 14^b$	....	10 ± 2	29 ± 5
C	7.7	92 ± 14	65 ± 4	8 ± 2	-43 ± 5
D	8.6	53 ± 14	68 ± 7	5 ± 2	-31 ± 5
E	9.3	63 ± 14	68 ± 6	12 ± 2	15 ± 5
D+E		58 ± 11	68 ± 5	8 ± 2	23 ± 5
C+D+E		70 ± 9	67 ± 3	8 ± 2	26 ± 5
HS	10.3	$< 13^b$	....	9 ± 2	37 ± 5

[a] Electric field vector position angle.
[b] 2σ upper limit.

Table 3
Spectral Indices ($F_\nu \propto \nu^{-\alpha}$) of Jet Features

Feature	α_R^a	α_O	α_X^a
α	0.75 ± 0.10	-0.16 ± 0.09	0.9 ± 0.4
$\alpha_{\rm Radio}$	0.75 ± 0.10	0.5 ± 0.3	
A	0.67 ± 0.11	0.1 ± 0.2	$1.1^{+0.3}_{-0.6}$
B	0.81 ± 0.13	1.0 ± 0.1	$1.1^{+0.2}_{-0.3}$
C	0.66 ± 0.09	2.6 ± 0.9	$0.5^{+0.3}_{-0.2}$
D	0.71 ± 0.08	2.3 ± 0.9	0.5 ± 0.5
E	0.82 ± 0.09	0.5 ± 0.90	$1.3^{+0.6}_{-0.5}$
HS	0.85 ± 0.08	1.6 ± 0.3	$0.7^{+0.9}_{-0.7}$

[a] See Sambruna et al. (2006)

2.7. Radio Observations

We obtained NRAO[18] Very Large Array (VLA) observations of PKS 1136−135 at 8.5 and 22 GHz. At 22 GHz, about 2.3 hrs total integration was obtained during a 24 hr observing run from 2002 May 27-28 in the hybrid BnA-array (program AC641). A full description of these data and the reduction procedures was presented in Cheung (2004). At 8.5 GHz, we obtained about

7.5 hr of exposure on PKS 1136−135 on 2003 November 8 in the B-array (AC689). The total intensity data from both frequencies were published in Sambruna et al. (2006) and Uchiyama et al. (2007), and the polarization data are newly presented here to compare to the optical results. The phase calibrator used in both experiments was 1127−145 and the flux density scale was set using 3C 48 (22 GHz) and 3C 286 (8.5 GHz). For polarization calibration, leakage terms in the 22 GHz observing run were calibrated using observations of two bright point dominated sources (1354+195 and 3C 454.3) observe;d over a wide range of parallactic angles. In the 8.5 GHz run, the leakage terms were determined using the unpolarized source OQ208 and were found to be consistent with those derived from the 1127−145 scans. Both experiments used observations of 3C 286 to set the absolute electric vector position angle (EVPA).

2.8. Spitzer Infrared Observations

Photometric data for the jet knots with the *Spitzer* IRAC 3.6 and 5.8 μm arrays are taken from Uchiyama et al. (2007), in which IRAC observations carried out on 2005 June 10 (*Spitzer* program ID 3586) were analyzed. Since the separation of adjacent knots is typically $\sim 1''$, comparable with the PSFs of the IRAC at 3.6 μm, the infrared images were fitted with a series of the PSFs located at the knots, after subtraction of the PSF wings of the quasar core. It was difficult to measure fluxes individually from knots C, D, and E, so a combined flux was reported for them (referred to as knot CDE) in Uchiyama et al. (2007).

3. IMAGING RESULTS

3.1. Jet Morphology and Aperture Photometry

Our F555W Stokes I image is a factor of several deeper than the *HST* images previously obtained by Sambruna et al. (2006). A total of seven knot regions are firmly detected in the optical. We list flux densities for these regions in Table 1, not only in our F555W image but also in other *HST* observations (§ 2.5) as well as in archival observations with the *Chandra* X-ray Observatory (§ 2.6), VLA (§ 2.7) and *Spitzer* Space Telescope (§ 2.8). Each of the archival datasets was published previously, with photometry (Sambruna et al. 2006; Uchiyama et al. 2007). However, our results dif-

fer significantly from those published in Sambruna et al. (2006). This includes improved region definition and galaxy and PSF subtraction (which was not done by those authors). These have led us to improve significantly on the results of Sambruna et al. (2006) using their data. We can confidently claim detection of all knot regions in the F814W images, whereas Sambruna et al. (2006) only published 3σ upper limits for some. We agree with Sambruna et al. (2006)'s result of non-detections of most of the fainter knots in F625W and F475W. In Table 2, we give optical polarization properties for the jet components in apertures shown in Figure 1. Table 3 gives spectral indices in radio, optical and X-ray for these jet features.

Figure 1 shows the *HST* image with the regions used for photometry overplotted. In Figure 2a, we show the *HST* polarization image of PKS 1136−135 as greyscale. The radio 8.5 GHz image is shown in contours, with polarization vectors representing the degree of polarization and direction of the inferred magnetic field. The contours and vectors are shown with the 8.5 GHz radio image overplotted in greyscale. The polarization features in this image are discussed in the next sub-section. Figure 2b shows the inverse of this overlay, with the radio image in greyscale and contours and vectors representing the degree of polarization and inferred magnetic field direction seen on the *HST* image. Figure 3 shows the *Chandra* X-ray image in color, with contours from the radio (blue) and *HST* (green) images overplotted. Finally, Figure 4 shows an overlay of the *HST* F555W image with the higher-resolution, 22 GHz radio image. These overlays enable us to make the first high-quality assessment of the optical morphology of the knots and compare them in detail to what is seen in other bands.

Virtually every jet region is extended in our deep F555W image. Knot α is revealed to be more than an arcsecond long. The brightest X-ray and optical emission comes predominantly, but not entirely from the upstream portion of the knot, while the radio emission comes almost entirely from its downstream end. For this reason, we measured the flux in knot α from two regions, one restricted to the region seen in optical, and the second restricted to the region seen in radio (called α_{Radio} in Tables 1-3). These two regions will also be broken out in our discussion of the broad-band spectrum (Sections 4.2-4.3) of jet regions. Also of note is the fact that the optical and X-ray emission from knots A and B is not co-located with the radio maxima, with the maxima in the optical and X-ray being located upstream (i.e., closer to the quasar) than the maxima in the radio. These features are also much more compact in the optical than in the radio, and have been noted before in other jets across a wide variety of luminosity classes (e.g., PKS 1127−145 – Siemiginowska et al. 2007, 3C 353 – Kataoka et al. 2008, Cen A – Hardcastle et al. 2007, and M87 – Perlman & Wilson 2005) The optically seen region of knot C also appears to have a different morphology in the optical than in the radio, with emission being extended along a quasi-linear feature inclined at about 45° angle from the local jet direction (Figure 4). It is unclear what this feature represents, but when combined with the bend that is observed at knot D the jet in this region appears to have a coiled appearance in the optical. A look at the 22 GHz radio image also reveals
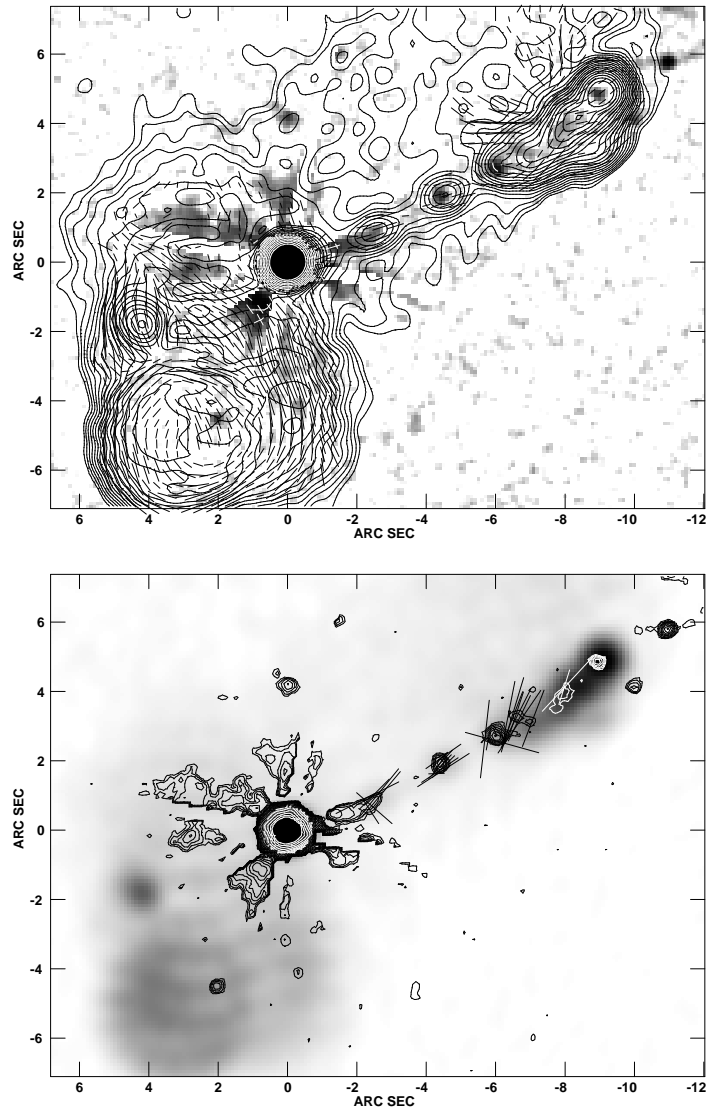

Figure 2. At top (Figure 2a), the Galaxy subtracted *HST* F555W Stokes I image of the PKS 1136−135 jet, shown with contours and polarization vectors taken from the radio 8.5 GHz image. At bottom (Figure 2b), the 8.5 GHz Stokes I image image of the PKS 1136−135 jet, shown with contours and polarization vectors taken from the galaxy-subtracted *HST* F555W Stokes I image. In both panels, the size of the polarization vector indicates the degree of polarization, with a 1 arcsecond long vector representing $\Pi_{\mathrm{Radio}} = 40\%$. The direction of the vectors indicates the direction of the inferred magnetic field (i.e., 90 degrees from the values reported in Table 2). The contours are spaced by multiples of $\sqrt{2}$. See §§ 3.1, 3.2 for discussion.

a coiled appearance in this region, but with a second region in knot C, not seen in the optical, that is inclined at a $\sim 90°$ angle from the northern one, converging in a "V" shape at the downstream end of the two regions. The optical and X-ray images show the same decrease in flux with distance from the core from knot B to knot E; however, the optical flux from the hotspot is considerably brighter relative to knots D and E than seen in the X-rays.

3.2. *Polarimetry*

As already mentioned, Figure 2 shows the comparison of radio and optical polarimetry of the PKS 1136−135
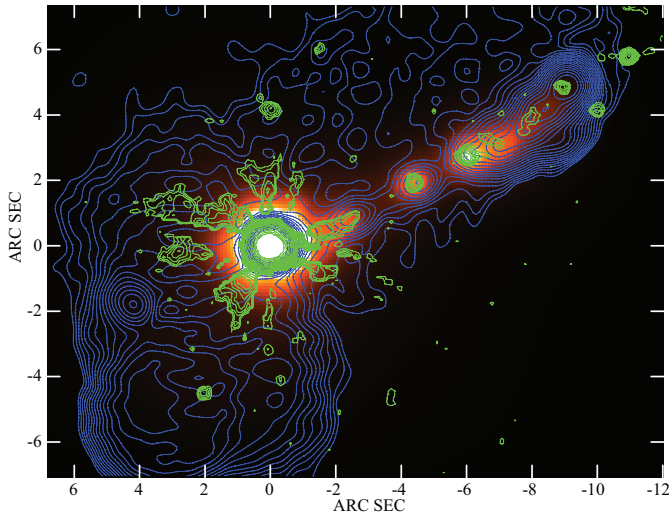
Figure 3. The *Chandra* X-ray image of the jet of PKS 1136−135 (color), with contours taken from the *HST* F555W data (green) and radio 8.5 GHz data (blue). The differences in morphology between the three bands is apparent. See §§ 3.1, 3.2 for discussion.
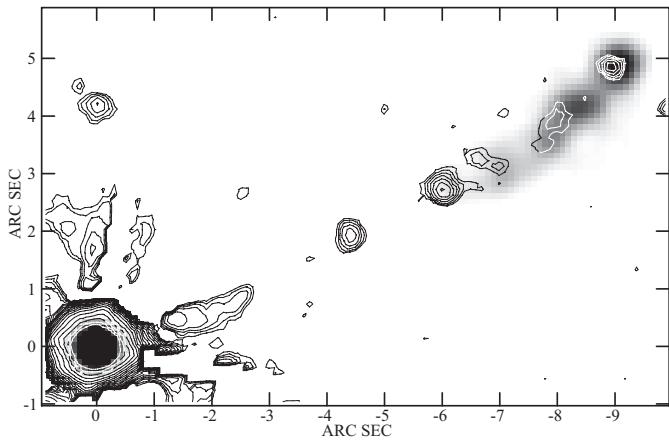

Figure 4. The 22 GHz, VLA A-array image is shown, in greyscale, with contours taken from the *HST* F555W image.

jet. The majority of the radio-bright knots in the jet (Figure 2b) are seen to be significantly polarized in the optical, with some regions having values of Π consistent with the theoretical maximum of ∼ 70% for a perfectly ordered magnetic field. The polarization vectors display definite structure, with a rotation of about 20° in χ seen between knot A and the knot C-D-E complex.

The radio polarization map is also interesting. The polarization in the jet interior is considerably lower, typically 5-10%, than seen at the northern and southern edges of the jet, where polarizations of 20-30% are seen. This trend, which is commonly seen in other quasar jets (e.g., Roberts, Wardle & Marchenko 2013) can be seen everywhere that the jet is resolved across its width in the 8.5 GHz polarization map. Even aside from this trend, the polarization of all jet regions is lower in the radio than in the optical, with the difference being a factor of three in knot A and a factors of 5-20 in knots C, D and E.

The orientation of the inferred magnetic field vectors (Table 2, Figure 2a) in the radio is generally aligned with the local jet direction, with the main differences being in knot B, which displays a 90° flip in the magnetic field direction at its upstream end, and in knot C, where the

vectors change direction by about 70° (Table 2; see also below). In the knots where significant polarizations are detected in both bands, we see significant differences in the inferred magnetic field direction of the radio and optical emission. In knot A, these differences may not be statistically significant because of the fact that the northern and southern ends of the knot have the same PA as seen in the radio. Higher resolution radio data are needed to resolve this issue. The differences are very significant, however, in knots C, D and E, as can be seen in Table 2 and also by comparing Figures 2a and 2b. Interestingly, in knots C and D the inferred magnetic field direction in the optical appears to be oriented 90° from the feature seen in the optical, with a PA more similar to the southern feature not seen in the optical. By comparison, the radio polarization map in this region shows near-zero polarization, perhaps due to cancellation of vectors from the two "arms" of this V-shaped region, which (as can be seen from the regions north and south of the optically bright feature) have polarization vectors that differ in direction by 90°. Also of note here is knot B, which in the radio map shows a radio position angle different from the dominant jet direction by about 60°. By comparison, in the optical knot B is formally not polarized, but a closer look at the vectors on Figure 2 reveals that this is so only because there appear to be multiple magnetic field orientations in that region, leading to a non-significant results when the Stokes parameters are added.

Another notable feature in the radio map is the high polarization and complex characteristics of the southern lobe and hot spot, as well as the apparent "sheath" to the north of the jet. These regions, which are not seen in the optical image, display very similar X-ray and radio morphologies. The northern "sheath" displays a diffuse morphology. The radio polarization vectors in this region, where seen, are oriented very nearly north-south, suggesting a flow out of the jet, perhaps similar to the sheath suggested for 3C 345 and other jets (Roberts, Wardle & Marchenko 2013). By contrast, in the southern lobe the morphology in the radio is dominated by three fairly bright features. The first of these is a hotspot about 4.5″ to the southeast of the quasar that is highly polarized (∼ 40%) and displays a magnetic field oriented about 10° from north-south, features that are strikingly different from those seen in the northern hotspot. The second dominant feature of the southern radio structure are two bubble-like features that are edge brightened and display higher polarizations around their edges (about 30%), with inferred magnetic field vectors that are correlated with the position angle of the local "wall" of the bubble. Much lower polarizations are seen within the bubble interior as well as in the region between the hotspot and bubble, where the polarization is consistent with zero.

4. DISCUSSION

The optical and X-ray emission from the PKS 1136–135 jet has been modeled with both synchrotron and IC/CMB models. Early work in Sambruna et al. (2002) based on a 10 ks *Chandra* observation and a single wide-band *HST* image, noted that knot A had a rather different broadband SED than other components in the PKS 1136–135 jet. These characteristics led them to favor the synchrotron model for the X-ray emission of

knot A but suggest that other mechanisms prevailed in the other knots. Later work (Sambruna et al. 2006; Tavecchio et al. 2006) based on a much deeper *Chandra* image and three *HST* images, ruled out the simple, one-component synchrotron model fit of Sambruna et al. (2002), and favored the IC/CMB mechanism for the X-ray emission of all the jet components. Uchiyama et al. (2007), however, presented a viable alternative interpretation for the X-ray and optical emission as synchrotron emission from a second, high-energy particle population.

In this light, the detection of high optical polarization in four regions of the PKS 1136–135 jet is highly interesting, particularly since recent work (McNamara et al. 2009; Uchiyama 2008; Uchiyama & Coppi 2013) predicts that IC/CMB emission should be unpolarized, reflecting the unpolarized nature of the seed photons. This is the first clear detection of high optical polarization in any quasar jet region, although in the 3C 273 jet early *HST* observations(Thomson et al. 1993) found similarly high polarizations that were inconsistent with much higher signal-to-noise ground-based observations(Röser & Meisenheimer 1991), and cannot be explained by just the difference in resolution. Th It has important implications for the origin of the high-energy emission in this jet, The high polarization that we measure in the optical jet of PKS 1136-135 has important implications for the origin of the high-energy emission, as discussed below. We concentrate particularly on knot A, which is the most challenging case, although we will also discuss the other jet regions in depth.

4.1. *Implications of the High Optical Polarization of the Jet Regions*

IC/CMB radiation by highly relativistic electrons with $\gamma \gg 1$ should be unpolarized. If instead the scattering electrons are cold ($\gamma \simeq 1$), the emission is in the regime of "bulk Comptonization" and it is in principle highly polarized (Begelman & Sikora 1987). To produce IC/CMB radiation at optical wavelengths, the scattering electrons need to be only mildly relativistic, with $\gamma \sim 1$–3. Here we investigate whether polarized, bulk IC/CMB emission could explain the high polarizations we detect. To calculate the intensity and polarization of the IC/CMB emission, we follow the prescription presented in Uchiyama & Coppi (2013). The model is described by the electron energy distribution $n_e(\gamma)$, a knot radius in the jet frame of reference (r_b), the bulk Lorentz factor of the jet (Γ), and the Doppler factor of the jet (δ). We adopt $r_b = 1$ kpc, which is unimportant when we calculate polarization. It is a common practice to assume a power law for the energy distribution of the electron density:

$$n_e(\gamma) = \begin{cases} k\gamma^{-s} & \text{for } \gamma \geq \gamma_{\min}, \\ 0 & \text{otherwise,} \end{cases} \quad (7)$$

where we adopt $s = 2.4$ (Uchiyama et al. 2007) and $\gamma_{\min} = 1.2$. We set k by assuming that the X-ray flux is attributable to the IC/CMB emission (see § 4.2).

In Figure 5, the photometric and polarimetric data for knot A are compared with the IC/CMB models with $\Gamma = 20$ and 40. We consider two cases of the Doppler factor, $\delta = \Gamma$ and $\delta = \Gamma/2$, for an assumed value of Γ. Generally, the case of $\delta = \Gamma/2$ provides a higher polarization degree than $\delta = \Gamma$, since the scattering angle in the jet frame

is optimal in the former case. The highest degree of polarization is $\Pi_{\max} = 26\%$ for $\delta = \Gamma/2$ and $\Gamma = 40$, and the position of the peak polarization shifts toward higher frequencies for higher Γ. At the *HST* band, the polarization degree ranges from $\Pi \simeq 12\%$ to $\Pi \simeq 25\%$. The *HST* observations presented in this paper give $\Pi = 37 \pm 6\%$. This can be reconciled at the 2σ level with the IC/CMB model for $\Gamma \simeq 40$, $\delta \simeq 20$ and $\gamma_{\min} \lesssim 1.2$, but is inconsistent with the lower Γ and lower δ models. We note that the polarization vector measured with the *HST* is close to perpendicular to the jet axis, and therefore the polarization direction of the IC/CMB emission roughly coincides with that of the *HST* measurement.

The parameter space allowed for the IC/CMB model is thus tightly constrained by the optical polarization measurements, and is restricted to a very high jet $\Gamma \geq 40$ and beaming parameter $\delta \sim 20$. The large value of Γ is required by (a) the need to shift the lowest end of the inverse- Compton "hump" into the optical (these photons would have seed electrons in the bulk, thermal tail of the EED, and would otherwise peak in the near-to-mid infrared, as discussed in Georganopoulos et al. 2005), and (b) the need to beam the IC/CMB sufficiently so that the bulk Compton emission dominates over the exponential synchrotron tail. The required beaming parameters also limit us to a viewing angle within 3° of the jet axis. Finding such a combination of jet parameters purely by chance is unlikely. For example, one can calculate the chance probability of finding a single jet with $\Gamma > 40$ (see below) in MOJAVE, assuming that the Lorentz factors of the sample range from 1.25 to 60 with a power-law index of $k = -1.5$ (Lister et al. 2009; Cara & Lister 2008), to be 3.8%. While such a probability is not prohibitively low, we would expect that such a source would have properties typical of other high-δ sources, e.g., a flat radio spectrum, high integrated optical polarization and OVV "blazar" type variability, neither of which is present in PKS 1136−135.
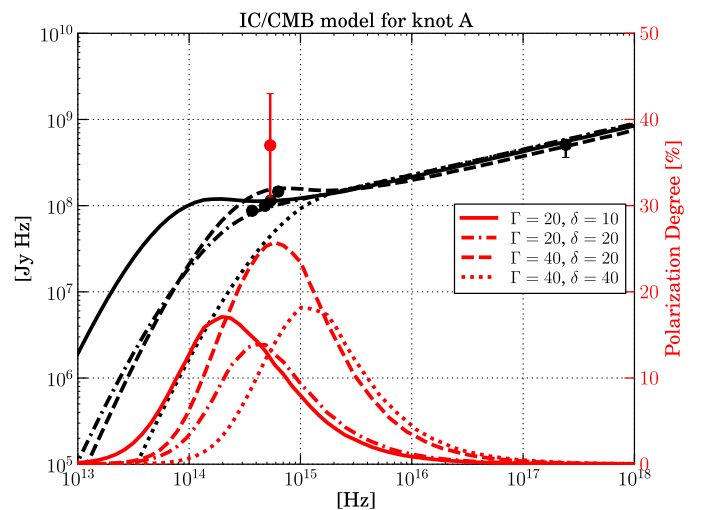

Figure 5. Intensity (black curves) and polarization degree (red curves) of the IC/CMB emission from a relativistic jet as a function of observing frequency. Data points present the *HST* results for knot A obtained in this paper. We show plots for jet bulk Lorentz factor $\Gamma = 20$ and 40, with beaming factor $\delta = \Gamma$ and $\delta = \Gamma/2$. See § 4.1 for discussion.

Other knots are also interesting to discuss in this regard. Knots B and α, which have fairly similar SEDs to that seen in knot A but low ($< 15\%$) optical polarization and steeper optical spectrum, do not challenge existing models strongly so the polarization data cannot further constrain its optical-to-X-ray emission mechanism. Both the IC/CMB and synchrotron models remain plausible for knots B and α. Knots C, D, and E, by contrast, have high optical polarization. Of these, two (knots C and D) have steep optical spectra ($\alpha_O \sim 2.5$) and optical-to-X-ray SEDs (Sambruna et al. 2006) consistent with optical-to-X-ray emission originating in synchrotron radiation from the same population of particles responsible for the lower-frequency (radio through IR) emission. The third of these (knot E) has α_O very similar to what is seen in the radio-through IR, suggesting that its optical emission originates in the same electron population as the radio through IR emission, and additionally a much higher break frequency than seen in the other knots.

4.2. *Modeling of the Spectral Energy Distribution*

Our observations place tight limitations on the parameter space available for synchrotron-inverse Compton emission models of knot A. Taking into account the requirements of high polarization, we now fit a synchrotron-inverse-Compton model to the multi-wavelength data for knot A (Table 1). We follow the prescription used in Perlman et al. (2011) for setting values of jet Γ, δ and viewing angle θ and attempt to match the observed broad-band emission. The hard optical spectrum of knot A is quite constraining in this regard. For example, using the low end of the range of Γ values allowed by the polarization modeling done in § 4.1 results in a flat optical spectrum, and also does not allow us to pick up the peak of the polarized emission, both necessary given these observations. We therefore found it necessary to direct the modeling towards higher values of Γ and use $\delta = \Gamma/2$ to maximize the polarized flux. This further restricts the region of parameter space open to an IC/CMB model.

As shown in Figure 6, it is possible to fit the broadband SED of the X-ray bright knot A with both a synchrotron and an IC/CMB model. The IC/CMB fit (top) requires a bulk Lorentz factor $\Gamma = 40$ and a Doppler factor $\delta = 20$ (i.e., $\theta = 2.48°$). This is a much more extreme set of parameters than previously required for the PKS 1136–135 jet in the IC/CMB model (Sambruna et al. 2006).

A simple power law electron energy distribution (EED) cannot accommodate the data. The reason for this is that a single power law EED that fits the radio would produce an IC/CMB spectrum that would be very hard and, if fitted the X-ray flux, would extend from there below the observed optical fluxes. For this reason we adopted a broken power law that is harder *above* a break energy: $n(\gamma) \propto \gamma^{-2.7}$ for $\gamma_{min} \leq \gamma \leq \gamma_{break}$ and $n(\gamma) \propto \gamma^{-2.3}$ for $\gamma_{break} < \gamma \leq \gamma_{max}$, with $\gamma_{min} = 1.6$, $\gamma_{break} = 160$, and $\gamma_{max} = 3 \times 10^5$. Such a break, with the EED hardening above a given energy, although not usually discussed in the literature, is generally expected at the energy where the high energy power law component of the EED starts to dominate over the low energy relativistic Maxwellian component, as relativistic particle-in-cell simulations show (Spitkovsky 2008). It also ne-

cessitates a slightly higher γ_{min}, as the lower value of § 4.1 would overproduce the optical-UV tail of the high-energy component. The jet kinetic power, assuming one cold proton per lepton, is ~ 34 times the Eddington luminosity of a 10^9 M$_\odot$ black hole. For a projected jet length of $\approx 11''$ and jet orientation $\theta = 2.48°$ (see above), the deprojected length of the jet is 1.63 Mpc, comparable with the largest known jets (Konar et al. 2004).

In the bottom panel of Figure 6 we plot a two-synchrotron component SED for knot A. For this representation we chose $\Gamma = \delta = 2$, corresponding to a jet angle to the line of sight of $\theta = 30°$. The first population of electrons, reproducing the radio to optical SED is a power law with $\gamma_{min,1} = 100$, $\gamma_{max,1} = 7 \times 10^5$, electron index 2.4 and power $L_{e,1} = 1.2 \times 10^{45}$ erg s^{-1}. The second component reproducing the optical to X-ray SED, which could form as a result of a continuous acceleration piling up radiating ultra relativistic electrons around the maximum energies available in the acceleration process (e.g., Stawarz & Petrosian 2008) is a power law with $\gamma_{min,2} = 3 \times 10^6$, $\gamma_{max,2} = 2 \times 10^8$, electron index 2.0 and power $L_{e,2} = 2.4 \times 10^{43}$ erg s^{-1}.

The magnetic field set to the equipartition value is $B = 4.7 \times 10^{-5}$ G. The jet kinetic power, assuming one cold proton per lepton, is $L_{jet} = 8.8 \times 10^{45}$ erg s^{-1}, $\sim 7\%$ of the Eddington luminosity of a 10^9 M$_\odot$ black hole. The deprojected length of the jet is 140 kpc.

This modeling of the SEDs shows that the IC/CMB model faces significant issues, as one needs very high beaming factors and small jet viewing angle to push IC/CMB from the $\gamma \sim 1$ electrons to high enough frequencies to explain the high polarization observed in the optical. However, given that PKS 1136−135 does not exhibit properties typical of blazars, such as rapid variability, flat radio spectrum and high core polarization (§ 1), these parameters are not favored. Thus, while the IC/CMB model for the X-ray emission is restricted to a small and unlikely range of parameter space, it is not completely ruled out.

4.3. *An additional diagnostic: the slope of the optical-UV spectrum*

Further progress can be made to narrow down the constraints on all the emission models by follow-up *HST* observations, which would allow further study of their optical-UV spectral shapes. In knot A, this could strengthen further the case against IC/CMB. This is based on the different slopes the inverse Compton and synchrotron low energy spectral tails have. The low energy tail of the X-ray component, produced by the lowest energy electrons of the EED, will have a spectral index $\alpha = -1/3$ for the synchrotron and $\alpha = -1$ for the IC/ CMB mechanism (e.g., Stawarz & Petrosian 2008; Dermer et al. 2009). If this tail extends to the optical - UV part of the spectrum, a measurement of the spectral index can be used to identify the emission mechanism. In the case of PKS 1136−135 the optical-UV spectrum of knot A is indeed hard and is part of the low energy tail of the X-ray component (see Figure 6).

The existing fluxes (from F814W, F625W, F555W and F475W) cover a factor of less than 2 in frequency. We plot in Figure 7 the three two-point spectral indexes we form from these fluxes. As can be seen, the spectrum
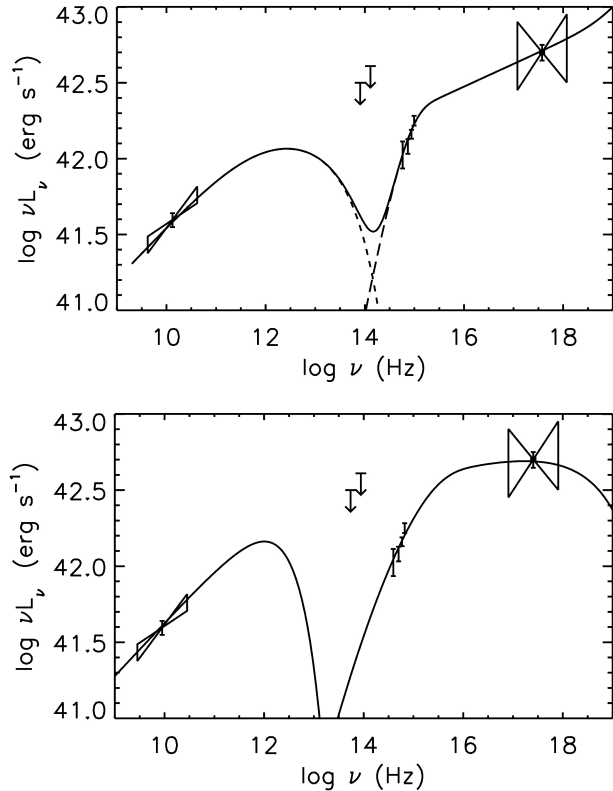
Figure 6. Fits of the knot A data of PKS 1136−135 with the IC/CMB (top) and two-synchrotron component (bottom) models. Both fits are reasonably good. They correspond, however, to extremely different jets (see text).
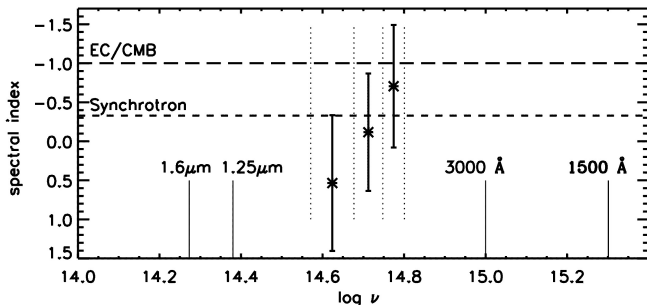

Figure 7. The three two-point spectral indexes of knot A of PKS 1136−135. The long and short dash horizontal lines represent the spectral index expected from the low energy tail of IC/CMB and synchrotron emission respectively. The thin vertical dotted lines mark the four wavelengths for which we have data. The four wavelengths at which future HST observations could extend the spectrum are also shown.

appears to harden with frequency. This suggests that at low frequencies the observed flux is the sum of the hard low energy tail of the X-ray component and the soft high energy tail of the radio - IR - optical synchrotron component. As we move to higher frequencies the contribution of this soft tail decreases and the spectral index we observe is closer to the actual spectral index of the low energy tail of the X-ray component. To exclude an emission mechanism we need the observed spectral in-

dex at any part of the optical-UV-spectrum to be harder than −1/3 for synchrotron and −1 for IC/CMB. Our existing data do not permit this, although the hardening of the spectrum at higher frequencies leaves open the possibility that at UV energies it may be possible to exclude the synchrotron mechanism. This would force us to accept IC/CMB with all of its important consequences of fast and powerful jets. On the other hand, the spectral index from the three highest energies (F625W, F555W and F475W) is 0.37 ± 0.20, which is in agreement with the synchrotron case. Additional HST observations at $1.6 \, \mu m$, $1.25 \, \mu m$, 3000 Å and 1500 Å, would be extremely useful in characterizing the IR-optical-UV spectrum and constraining further the optical-UV-X-ray emission mechanism.

Future observations can also narrow down the constraints for the other knots. The spectrum of knot α is also consistent with either synchrotron emission from a second, high-energy electron population, but the constraints on IC/CMB radiation are much less severe because of its low optical polarization. Additional HST observations could allow us to detect a spectral break that could decide between these two interpretations. For knot B, the current data are consistent with either a significantly higher ν_{break} in the synchrotron emission or the optical emission could be from IC/CMB radiation. Both of these possibilities would be constrained by observations in the near-IR and UV, as each of these two models would predict spectral breaks that would be detectable either in the UV or near-IR. Finally, for knot E, if the optical emission is from the same electron population responsible for the radio-IR component, the observed X-ray flux and spectral index (Tables 2, 3) predict a steepening in its spectral index towards the UV.

4.4. *The Jet Power*

Another constraint on the nature of the observed optical and X-ray emission and also the nature of the jet can be achieved by looking at the jet power implied by such a model. In Figure 8 we show the result of modeling the power requirements for knot A, showing tracks for electron power, Poynting flux, leptons only and total for one proton per electron. To produce this plot we followed the prescription of Mehta et al. (2009) and Georganopoulos et al. (2005). In this plot we have required that the X-ray and radio power agree with the observations. As can be seen, for $20 < \Gamma < 50$ the leptonic power required is sub-Eddington. In particular, for the $\Gamma = 40$, $\delta = 20$ model discussed above, the leptonic power required is 3.1×10^{46} erg/s, about $0.3 \times$ the Eddington luminosity of PKS 1136−135's black hole. However, if we require one cold proton per lepton, the power requirement is much more extreme, about $10 \times$ Eddington. As discussed above, we do not favor this model for a variety of reasons, but if we go to a different region of parameter space which appears more reasonable given the observed properties of PKS 1136−135 (i.e., lower values of Γ and δ), the total power requirement goes up significantly and is in excess of Eddington even for a lepton only jet at $\Gamma < 10$. Furthermore, in such a case we could not reproduce the observed optical polarization as in that case the optical emission would have to come from IC/CMB with particles at higher Lorentz factors γ.
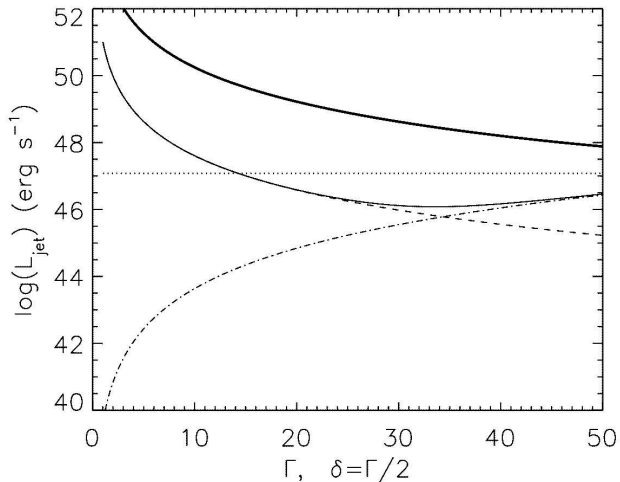
Figure 8. Power requirements for knot A, using the observed spectral energy distribution and the IC/CMB interpretation. Tracks are shown for the electron power (dot dashed line), the Poynting flux (broken line), the total power for leptons only (thin solid line) and the total power for one proton per electron (thick solid line). Beaming factor δ is constrained to be equal to $\Gamma/2$, but for a given Γ, the magnetic field required is then set by the ratio of radio to X-ray flux (see e.g., Perlman et al. 2011, and references therein). See § 4.2 for discussion.

The alternative to the IC/CMB model is to produce the optical and X-ray emissions in a second, high-energy synchrotron component. This model is attractive because one is not at all restricted in the choice of bulk Lorentz factors Γ or viewing angle θ since there is no requirement to produce the highly polarized optical emission with IC/CMB off the very lowest energy, $\gamma \sim 1$ particles. Such a model would easily explain the high polarizations we observe and also have the advantage of lowering the jet power requirement by approximately $\sqrt{m_p/m_e}$, as here the ratio of jet radio to X-ray luminosity would not be fixed for a given set of parameters.

5. CONCLUSIONS

The origin of the high-energy emission in quasar jets is a long-standing issue, dating back to the discovery of X-ray emission from the jet of 3C 273 (Willingale 1981). Early work (Harris & Stern 1987) found that it was difficult to interpret the X-ray emission as either an extension of the radio-optical emission or due to the synchrotron self-Compton process. Later work, following the launch of the *Chandra* X-ray Observatory, centered around IC/CMB emission (e.g., Schwartz et al. 2000; Celotti et al. 2001; Marshall et al. 2001). This process, like SSC, is attractive because it is mandatory – the mere presence of high-energy particles ensures emission from IC/CMB at some level. However, our ability to observe this component, combined with the strength of the component itself, is highly geometry dependent. In particular, for the IC/CMB component to dominate the observed X-ray emission, the jet must be strongly beamed, and remain relativistic for tens to hundreds of kiloparsecs from the active nucleus. In some objects, such as PKS 0637−752, where strong gamma-ray emission and/or other blazar properties are observed, as well as a lack of a continuous optical-to-X-ray component (see e.g., Mehta et al. 2009), this seems to be the leading hypothesis. However, in several objects, such as 3C 273 and

PKS 1136−135, the lack of evidence for strong beaming and the presence of optical to X-ray emission from a single spectral component, has reinvigorated the possibility that the X-ray and optical emission may be synchrotron emission from a second, high-energy population of electrons (Jester et al. 2006, 2007; Uchiyama et al. 2006).

The observations discussed in this paper argue strongly against the IC/CMB process as being dominant in the X-ray band, at least for the case of the jet of PKS 1136−135. While the SED of knot A shows that the X-ray and optical emission are clearly linked, the high polarization we observe in knot A and other components require a very highly beamed jet, with bulk Lorentz factor $\Gamma \geq 30$ and viewing angle within 3° of the jet axis. These constraints (much tighter than previous work; Sambruna et al. 2006; Tavecchio et al. 2006) are a result of the need for the polarized optical emission to come from the very lowest energy ($\gamma \sim 1$) electrons, as IC/CMB emission from higher energy particles would be unpolarized. They are also substantially tighter than typically required for the IC/CMB process, as where polarization data are not present there is no requirement for the observed optical emission (if any) to come from bulk Compton emission from $\gamma \sim 1$ electrons (as in the case of PKS 0637−752, Mehta et al. 2009). The required configuration is highly unlikely given the observed properties of PKS 1136−135, which has a steep radio spectrum and displays neither rapid variability or high integrated optical polarization, unlike blazars, the more typical, high-δ source. Furthermore, the energetic demands of such a jet are extreme: if we require one proton per radiating lepton, the jet power must be at least $10 \times$ the Eddington luminosity of PKS 1136−135's black hole, and such a configuration might result in Faraday depolarization in the radio (Jones & O'Dell 1977).

The observations presented here instead favor a more complicated story. While the IC/CMB process is mandatory, synchrotron emission from a second, high-energy particle population is the favored interpretation for knot A's X-ray emission, which is spectrally linked to the polarized optical emissions. Synchrotron emission is also required to explain the highly polarized optical emissions of knots C, D and E. Two of those knots (C and D) show optical spectra that are decreasing in νF_ν and do not appear spectrally linked to the X-ray emission. For those knots, we cannot use the optical polarization characteristics to infer conclusions about the nature of the X-ray emission. Knot E, however, has an SED much more similar to knot A and is also highly polarized. A similar explanation for its X-ray emission seems likely. The two-component synchrotron model, first suggested for the jet of PKS 1136–135 by Uchiyama et al. (2007), requires the high-energy particle population to be spectrally distinct from that seen at lower (radio-infrared) energies, but does not specify whether it is spatially co-located with the lower-energy one. Discriminating between these two possibilities requires further, high-angular resolution work, and while we do see significant differences between the X-ray, optical and radio morphologies (e.g., Figure 3), the resolution in the X-rays is insufficient to comment further.

REFERENCES

Baggett, S., et al. 2002, "HST WFPC2 Data Handbook", Version 4.0, ed. B. Mobasher (Baltimore: STScI)

Begelman, M. C., & Sikora, M. 1987, ApJ, 322, 650

Biretta, J. A., & McMaster, M. 1997, WFPC2 Instrument Science Report 97-11 (Baltimore: STScI)

Cara, M., & Lister, M. L. 2008, ApJ, 674, 111

Celotti, A., Ghisellini, G., & Chiaberge, M. 2001, MNRAS, 321, L1

Cheung, C. C. 2004, PhD thesis, Brandeis University

Dermer, C. D., Finke, J. D., Krug, H., Böttcher, M., 2009, ApJ, 692, 32

Dolphin, A. E. 2009, PASP, 121, 655

Dulwich, F., Worrall, D. M., Birkinshaw, M., et al. 2007, MNRAS, 374, 1216

Fanaroff, B. L., & Riley, J. M. 1974, MNRAS, 167, 31

Fruchter, A., Sosey, M., et al. 2009, "The MultiDrizzle Handbook", Version 3.0, (Baltimore: STScI)

Georganopoulos, M., & Kazanas, D. 2003, ApJ, 589, L5

Georganopoulos, M., Kazanas, D., Perlman, E., et al. 2005, ApJ, 625, 656

Georganopoulos, M., Perlman, E. S., Kazanas, D., et al. 2006, ApJ, 653, L5

Ghisellini, G., Celotti, A., MNRAS, 327, 239

Gough, B., 2008, GNU Scientific Library, Statistical Function Notes, http://bzr.savannah.gnu.org/lh/gsl/trunk/annotate/head/doc/statnotes.tex

Hardcastle, M. J., Birkinshaw, M., & Worrall, D. M. 2001, MNRAS, 326, 1499

Hardcastle, M. J., et al., 2007, ApJ, 670, L81

Harris, D. E., Stern, C. P., 1987, ApJ, 313, 136

Harris, D. E., Carilli, C., & Perley, R. 1994, Nature, 367, 713

Harris, D. E., & Krawczynski, H. 2006, ARA&A, 44, 463

Hook, R. N., Walsh, J., Pirzkal, N., & Freudling, W. 2000, in ASP Conf. Proc. 216, Astronomical Data Analysis & Software Systems IX, ed. N. Manset, C. Veillet, & D. Crabtree (San Francisco: ASP), 671

Jester, S., Röser, H.-J., Meisenheimer, K., Perley, R., et al. 2001, å, 373, 447J

Jester, S., Harris, D. E., Marshall, H. L., et al. 2006, ApJ, 648, 900

Jester, S., Meisenheimer, K., Martel, A. R., et al. 2007, MNRAS, 380, 828

Jones, T. W., O'Dell, S. L. 1977, ApJ, 214, 522

Kataoka, J., & Stawarz, L. 2005, ApJ, 622, 797

Kataoka, J., et a., 2008, ApJ, 685, 839

Konar, C., Saikia, D. J., Ishwara-Chandra, C. H., Kulkarni, V. K., 2004, MNRAS, 355, 854

Kraft, R. P., et a., 2005, ApJ, 622, 149

Krist, J. 1993, in ASP Conf. Ser. 52, Astronomical Data Analysis Software and Systems II, ed. R. J. Hanisch, R. J. V. Brissenden, & J. Barnes, 536

Krist, J., & Hook, R. N. 2004, "The Tiny Tim User's Guide", Version 6.3 (Baltimore: STScI)

Labita, M., Treves, A., Falomo, R., Uslenghi, M., 2006, MNRAS, 373, 551

Laidler et al, 2005, "Synphot Users Guide", Version 5.0 (Baltimore: STScI)

Lister, M. L., Cohen, M. H., Homan, D. C., Kadler, M., Kellermann, K. I., Kovalev, Y. Y., Ros, E., Savolainen, T., & Zensus, J. A. 2009, AJ, 138, 1874

Marshall, H. L., Harris, D. E., Grimes, J. P., Drake, J. J., Fruscione, A., Juda, M., et al. 2001, ApJ, 549, 167

McNamara, A. L., Kuncic, Z., & Wu, K. 2009, MNRAS, 395, 1507

McNamara, B. R., Nulsen, P. E. J., 2007, ARA&A, 45, 117

Mehta, K. T., Georganopoulos, M., Perlman, E. S., et al. 2009, ApJ, 690, 1706

Naghizadeh-Khouei, J., & Clarke, D. 1993, A&A, 274, 968

Pavlovsky, C., et al. 2005, "ACS Data Handbook", Version 4.0 (Baltimore: STScI).

Perlman, E. S., Biretta, J. A., & Zhou, F., et al. 1999, AJ, 117, 2185

Perlman, E. S., Biretta, J. A., & Sparks, W. B., et al. 2001, ApJ, 551, 206

Perlman, E. S., & Wilson, A. S. 2005, ApJ, 627, 140

Perlman, E. S., Padgett, C. A., Georganopoulos, M., et al. 2006, ApJ, 651, 735

Perlman E. S., Padgett, C. A., Georganopoulos, M., et al., ApJ, 708, 171

Perlman, E. S., Georganopoulos, M., Marshall, H. L., Schwartz, D. A., Padgett, C. A., Gelbord, J., Lovell, J. E. J., Worrall, D. M., Birkinshaw, M., Murphy, D. W.; Jauncey, D. L. 2011, ApJ, 739, 65

Poutanen, J., & Vilhu, O. 1993, A&A, 275, 337

Ramos Almeida, C., et al., 2011, MNRAS, 410, 1550

Rawlings, S., & Saunders, R. 1991, Nature, 349, 138

Roberts, D. H., Wardle, J. F. C., Marchenko, V. V., 2013, AJ, 145, 49

Röser, H. J. & Meisenheimer, K. 1991, A&A, 252, 458

Sambruna, R. M., Maraschi, L., Tavecchio, F., et al. 2002, ApJ, 2002, 571, 206

Sambruna, R. M., Gambill, J. K., Maraschi, L., et al. 2004, ApJ, 608, 698

Sambruna, R. M., Gliozzi, M., Donato, D., Maraschi, L., Tavecchio, F., Cheung, C. C., Urry, C. M., & Wardle, J. F. C. 2006, ApJ, 641, 717

Schwartz, D. A., Marshall, H. L., Lovell, J. E. J., et al. 2000, ApJ, 540L, L69

Serkowski, K. 1962, Advances in Astronomy and Astrophyscs, ed. Z. Kopal (New York and London: Academic Press), 1, 289

Siemiginowska, A., et al., 2007, ApJ, 657, 145

Sluse, D., et al., 2005, A&A, 433, 757

Spitkowsky, A, 2008, ApJ, 682, L5

Stawarz, L., Petrosian, V., 2008, ApJ, 682, 1725

Tadhunter, C., et al., 1993, MNRAS, 330, 977

Tavecchio, F., Maraschi, L., Sambruna, R. M., et al. 2000, ApJ, 544L, 23

Tavecchio, F., Maraschi, L., Sambruna, R. M., Gliozzi, M., Cheung, C. C., Wardle, J. F. C., Urry, C. M., 2006, ApJ, 641, 723

Thomson, R. C., Mackay, C. D., & Wright, A. E. 1993, Nature, 365, 133

Uchiyama, Y., Urry, C. M., Cheung, C. C., et al. 2006, ApJ, 648, 910

Uchiyama, Y., Urry, C. M., Coppi, P., et al. 2007, ApJ, 661, 719

Uchiyama, Y., 2008, Int. J. Mod. Phys. D, 17, 1475

Uchiyama, Y., & Coppi, P., et al. 2013 (in preparation)

Wall, J. V., Peacock, J. A., 1985, MNRAS, 216, 173

Wardle, J. F. C., & Kronberg, P. P. 1974, ApJ, 194, 249

Willingale, R., 1981, MNRAS, 194, 359

Wilson, A. S., Young, A., & Shopbell, P. 2001, ApJ, 547, 740

Worrall, D. M., 2009, A& A R, 17, 1

Worrall, D. M., Birkinshaw, M. B., 2005, MNRAS, 360, 926